

Supplementary information

Diffusion encouraged core-shell heterostructure $\text{Co}_3\text{Sn}_2@\text{SnO}_2$ anode towards emerging dual ion battery with high energy density

Tejaswi Tanaji Salunkhe,^a Abhijit Nanaso Kadam,^a Weldejewergis Gebrewahid

*Kidanu,^{a,b} Sang-Wha Lee,^a Tuan Loi Nguyen,^{*c,d} Il Tae Kim^{*a}*

^a Department of Chemical and Biological Engineering, Gachon University, Seongnam-si, Gyeonggi-do 13120, South Korea

^b Department of Chemical Engineering, Ethiopian Institute of Technology-Mekelle (EIT-M), Mekelle University, Mekelle, Tigray, 231, Ethiopia

^c Institute of Fundamental and Applied Sciences, Duy Tan University, Ho Chi Minh City 700000, Vietnam

^d Faculty of Environmental and Chemical Engineering, Duy Tan University, Da Nang 550000, Vietnam

*Correspondence

E-mail: itkim@gachon.ac.kr (I.T. Kim) and nguyentuanloi@duytan.edu.vn (T.L. Nguyen)

Material characterization

The crystal structure of as-prepared samples was assessed by X-ray diffraction (XRD) using Rigaku D/max 2200 (Japan) tool with monochromatic Cu K α radiation. Their surface morphology was observed by using scanning electron microscopy (SEM; Hitachi S-4700). Further details of morphology and structure of as-synthesized products was characterized by transmission electron microscopy (TEM) and high-resolution (HRTEM) by means of a Talos F200X instrument (Thermo Fisher Scientific). The energy dispersive X-ray spectroscopy (EDS) using the Talos F200X instrument and X-ray photoelectron spectroscopy (XPS, Kratos AXIS Nova) were used to investigate elemental composition and chemical state. Fourier-transform infrared (FTIR) spectra were recorded to understand the bonding nature as well as surface functional groups using a Perkin-Elmer spectrometer (Spectrum BX-II). The specific surface area of the as-prepared product was recorded using the Brunauer-Emmett-Teller (BET) nitrogen adsorption-desorption technique (ASAP 2020) and a Monora500i (ANDOR) micro-Raman spectrometer was used to record Raman spectra.

Electrochemical measurements

Working electrode films were fabricated by dissolving the active material, carbon black, and a poly (acrylic acid) binder at a weight ratio of 70:15:15 in ethanol and depositing the solution on copper foils. The deposited electrodes were dehydrated for 3 h in an air oven at 60 °C and subsequently for 12 h in a vacuum oven at 70 °C. CR2032-type coin cells were constructed in an Ar-filled glove box (moisture and oxygen less than 0.1 ppm) using electrodes containing 1.3–1.5 mg of the active material (Co₃Sn₂@SnO₂), lithium foil was employed as counter electrode, and the electrolyte consisting of 1.0 M LiPF₆ in ethylene carbonate (EC) and diethylene carbonate (DEC) (1:1 v/v). A polyethylene membrane was used as the separator. Galvanostatic charge–discharge testing was conducted at a current density of 100 mA g⁻¹ and rate performance was analyzed at 100 mA g⁻¹, 500 mA g⁻¹, 1 A g⁻¹, 3 A g⁻¹, and 5 A g⁻¹ using

a battery cycler (WBCS3000, WonAtech) in the range of 0.01–2.00 V (vs. Li/Li⁺). A ZIVE MP1 station was used to record Electrochemical impedance spectroscopy (EIS) in the frequency range from 100 kHz to 0.1 Hz at the 50th and 500th discharge–charge cycles. To evaluate the diffusion coefficients of the Li⁺ towards as-synthesized electrodes, cyclic voltammetry (CV) was conducted after two cycles over scanning rates of 0.1–1.0 mV s⁻¹ in the potential window of 0.01–2 V using a ZIVE MP1 station. The expanded graphite cathode was cast on the aluminum foil with a weight ratio of the active: polyvinylidene difluoride: conduction carbon (60:30:10) and dried in a vacuum oven at 70 °C for 12 h. A LIB half-cell with EG (cathode) and Li metal (anode) was cycled at 50 mA g⁻¹ in the range of 2–5 V. The ex-situ XRD and Raman measurement were conducted for EG cathode run at 10 mA g⁻¹ for the initial cycle. LDIB CR2032-type coin cells were assembled with EG/prelithiated Co₃Sn₂@SnO₂ as the cathode/anode with 1 M LiPF₆ in EC:DEC (1:1 v/v) as the electrolyte and the capacity of the LDIB was calculated using the weight of the anode. According to previous reports, the 1 M concentration of LiPF₆ in the electrolyte is enough high to provide sufficient Li⁺ and PF₆⁻ ions for electrochemical reactions for running the dual ion battery.¹⁻⁴ It is also noted that when the electrolyte concentration increases to more than 1 M, the LiPF₆ is hard to be fully dissolved in the solvent. Therefore, 1 M concentration of LiPF₆ in the electrolyte has been used in this work.

Synthesis method of the EG

In a typical procedure, pristine graphite (1 g) and ammonium bicarbonate (8 g) were subjected to the ball milling process in a ZrO₂ bowl (80 cm³) with ZrO₂ balls (diameters of 3/8 in and 3/16 in) at a ball to- powder ratio of 20:1. Then, the container was agitated at 300 rpm for 24 h. After that, the mixture was heated in a vacuum oven at 60 °C for 20 min in a sealed vial and subsequently cooled to room temperature to ensure sufficient ammonium bicarbonate-intercalated graphite. Thereafter, the intercalated graphite was put into a microwave (MW)

oven (WC-A201KW, 2.450 MHz, 700 W) for 60 s. Under MW, the precursor (graphite) was reacted rapidly, accompanied by lightening. On completion of the reaction, the product was heated in a muffle furnace at 500 °C for 15 min in air without any special treatment to completely remove the undecomposed ammonium bicarbonate.

The kinetics calculations

The relation of the peak current and the scan rate,

$$i = av^b \quad (S1)$$

$$\log(i) = b\log(v) + \log(a) \quad (S2)$$

Where,

i is measured current,

a is adjustment parameter,

b is indicative of the charge storage kinetics in the electrodes,

b can be calculated from the slope of the linearly fitted $\log(i)$ – $\log(v)$ plot, while a can be calculated by the intercept of the linear plot. When $b = 1$, the Li-ion process can be entirely dominated by the capacitive electrochemical process, whereas if $b = 0.5$, the route is a completely diffusion-controlled reaction. If b lies between 0.5 and 1, then both pseudo capacitive and diffusion processes exist together for Li-ion storage.

$$i(V) = k_1v + k_2v^{1/2} \quad (S3)$$

$$i(V)/v^{\frac{1}{2}} = k_1v^{\frac{1}{2}} + k_2 \quad (S4)$$

Where,

k_1v represents for the surface capacitive of current

$k_2\nu^{1/2}$ denotes the diffusion controlled contribution of the current

The intercept and slope of the linear plot of the $i/\nu^{1/2}$ vs $\nu^{1/2}$ at a specific potential determine the k_2 and k_1 values, respectively.

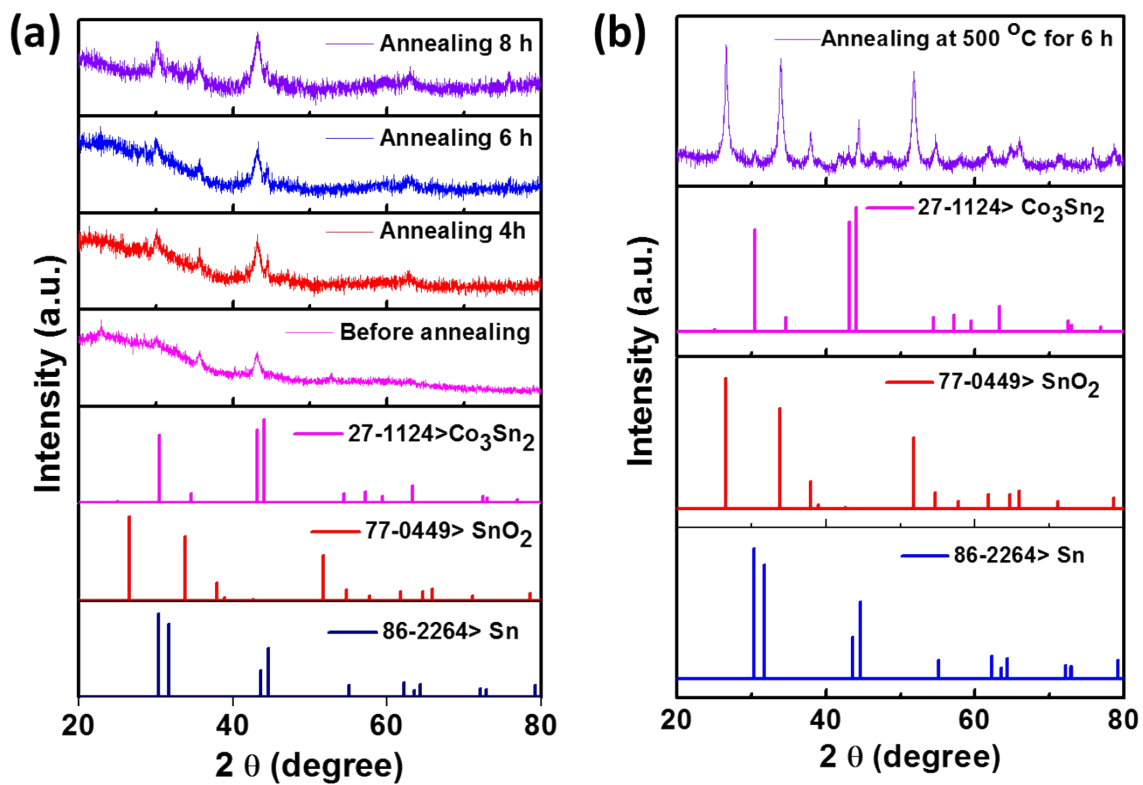


Fig. S1. (a) XRD patterns of as-prepared initial samples ($\text{Co}_3\text{Sn}_2@ \text{Sn}(\text{OH})_x$) annealed at different annealing times at 200 °C. (b) the XRD pattern annealed at 500 °C for 6h.

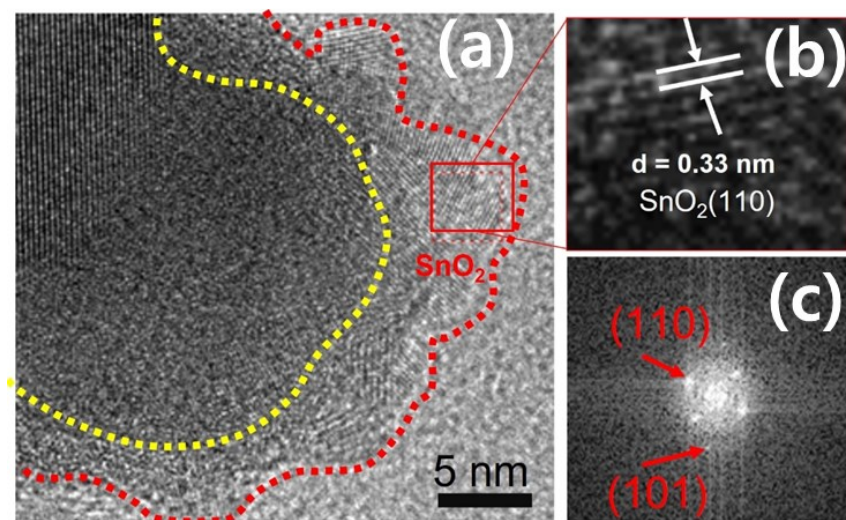


Fig. S2. (a) HRTEM image; (b) Enlarged HRTEM at SnO₂ shell; and (c) SAED pattern scanned at the edge of the shell for Co₃Sn₂@SnO₂-6h sample annealed at 500 °C for 6h.

HRTEM measurement for observing different lattice fringes of the core and shell of annealed sample at 500 °C for 6 h was performed (Sample discussed in **Fig. S1b**). As expected, the HRTEM image clearly shows two distinct phases comprised of Co₃Sn₂ core and SnO₂ surface layer (**Fig. S2(a)**). Importantly, the crystallinity of SnO₂ shell could be observed, which shows lattice fringes with d-spacing value of 0.33 nm attributing to (110) plane of SnO₂ (**Fig. S2(b)**). In addition, the SAED pattern of SnO₂ shell discloses the bright spots corresponding to the (110) and (101) planes of SnO₂ phase (**Fig. S2(c)**). These findings clearly support the formation of amorphous SnO₂ layer at lower temperature (200 °C).

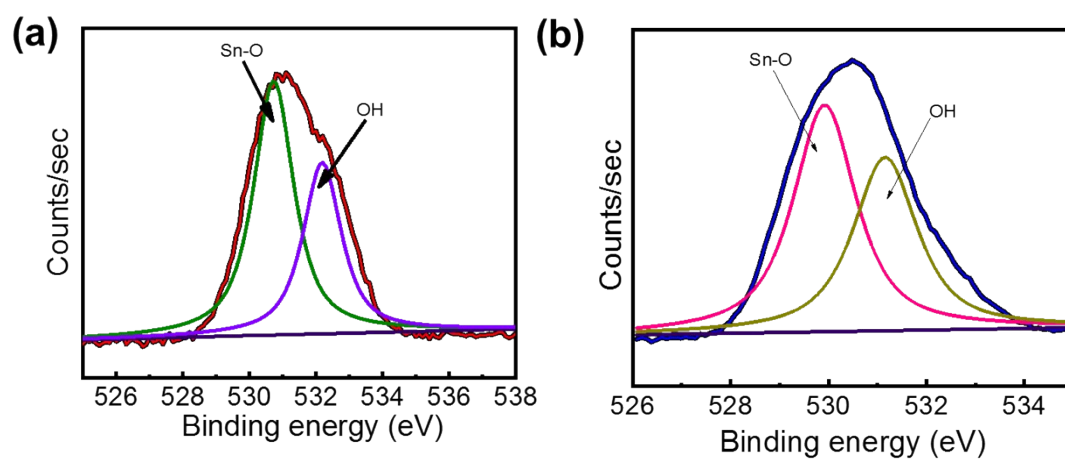


Fig. S3. High-resolution O1s spectra of $\text{Co}_3\text{Sn}_2@\text{SnO}_2\text{-6h}$ and $\text{Co}_3\text{Sn}_2@\text{SnO}_2\text{-12h}$ CSHs.

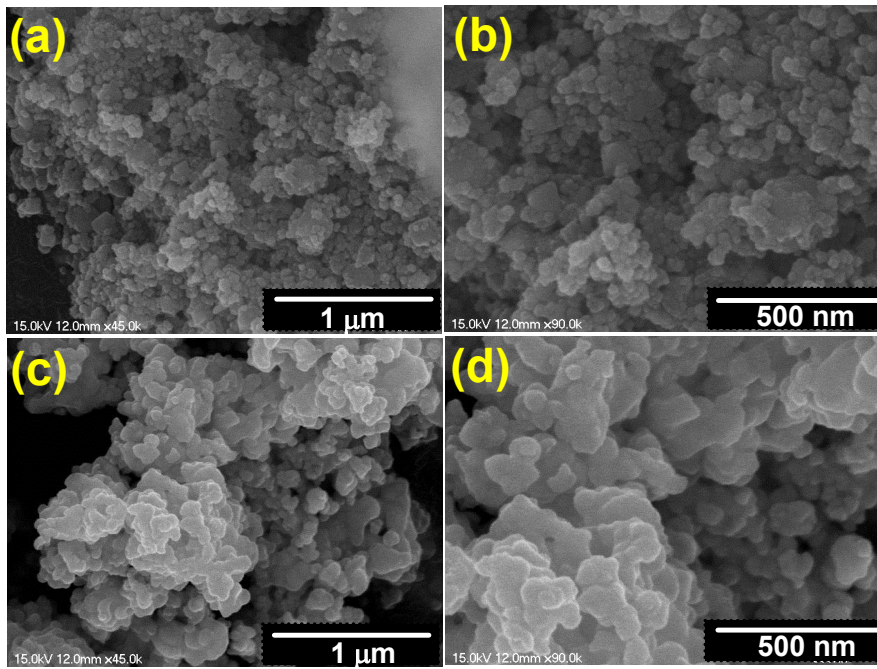


Fig. S4. SEM images of the $\text{Co}_3\text{Sn}_2@ \text{SnO}_2$ -6h CSHs (a-b) and $\text{Co}_3\text{Sn}_2@ \text{SnO}_2$ -12h (c-d).

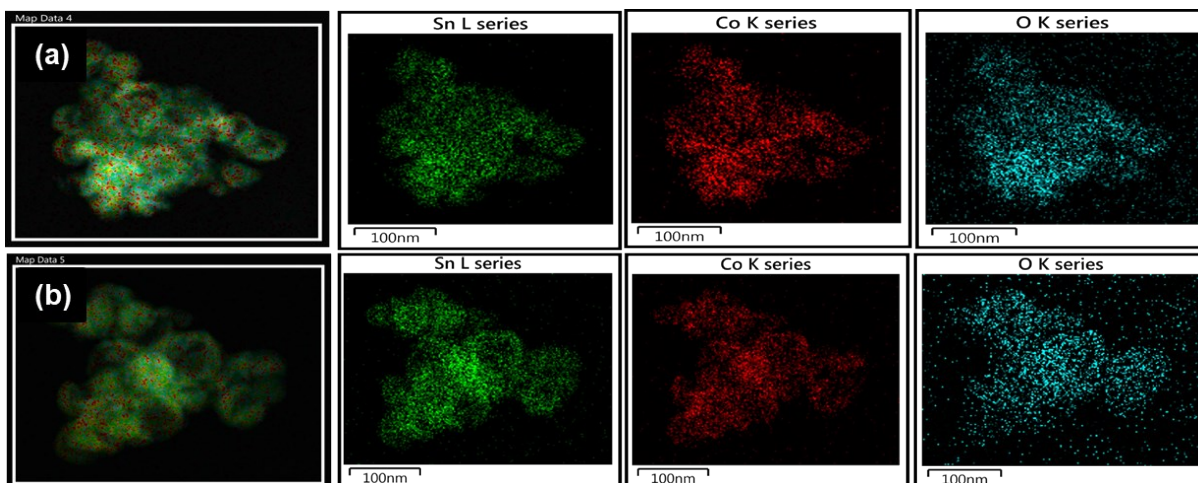


Fig. S5. Low magnification EDS maps of $\text{Co}_3\text{Sn}_2@\text{SnO}_2\text{-6h}$ CSHs (a) and $\text{Co}_3\text{Sn}_2@\text{SnO}_2\text{-12h}$ CSHs (b).

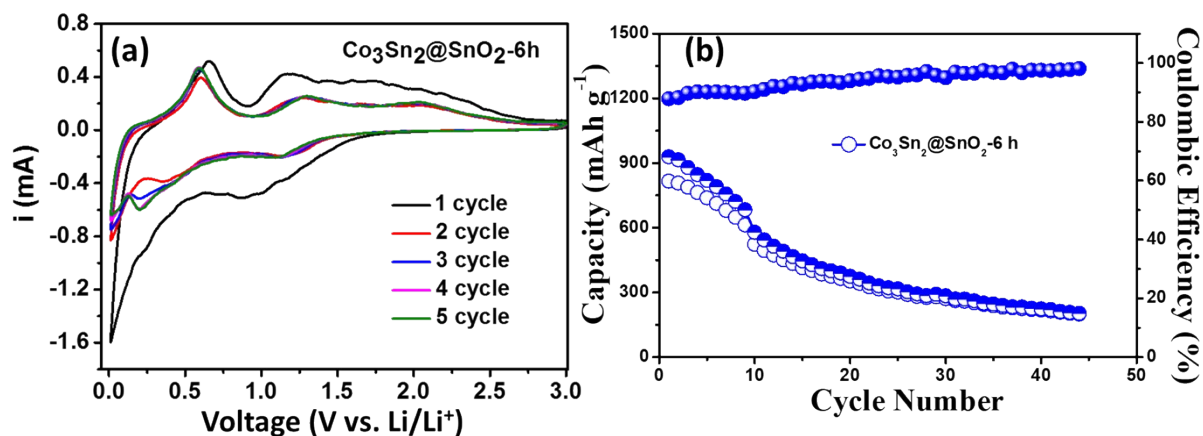
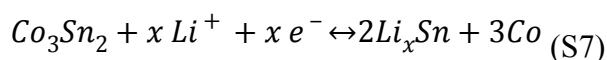
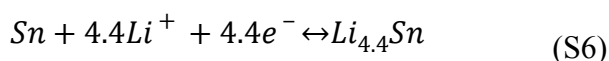
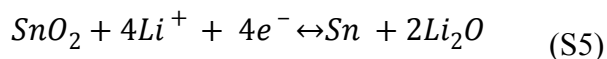


Fig. S6. (a) Cyclic voltammograms of $\text{Co}_3\text{Sn}_2@\text{SnO}_2\text{-6h}$ electrode and (b) Cyclic performance of $\text{Co}_3\text{Sn}_2@\text{SnO}_2\text{-6h}$ in the potential window of 0.01 to 3.00 V.

As discussed in the main text, the reversible reactions of Sn and SnO_2 with Li^+ ions occur below 2 V (Eq. S5, Eq. S6), while the reformation of Co_3Sn_2 phase happens at 2.10 V (Eq. S7).⁵ Therefore, when cycling between 0.01 to 3.00 V, $\text{Co}_3\text{Sn}_2@\text{SnO}_2\text{-6h}$ electrode exhibited high capacity values because of the reformation of Co_3Sn_2 at high voltage zone when comparing the cycling results from between 0.01 to 2.00 V. When cycling between 0.01 to 2.00 V, the reformation reactions of Co_3Sn_2 (Eq. S7) only happened partially, leading to lower capacity.



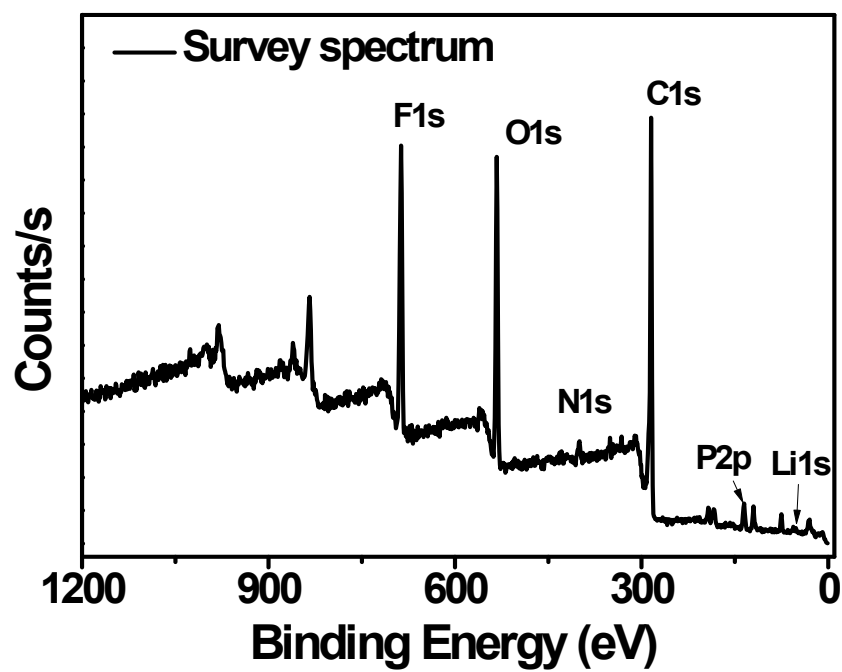


Fig. S7. *Ex-situ* XPS survey spectrum of EG cathode after fully charged condition.

Table S1. BET surface area, pore diameter and pore volume of $\text{Co}_3\text{Sn}_2@\text{SnO}_2$ -6h and $\text{Co}_3\text{Sn}_2@\text{SnO}_2$ -12h CSHs.

Sample	Surface area ($\text{m}^2 \text{g}^{-1}$)	Average pore diameter (nm)	Pore volume ($\text{cm}^3 \text{g}^{-1}$)
$\text{Co}_3\text{Sn}_2@\text{SnO}_2$-6h CSHs	35.33	6.49	0.0643
$\text{Co}_3\text{Sn}_2@\text{SnO}_2$-12h CSHs	15.37	20.35	0.0787

Table S2. EIS simulated results of $\text{Co}_3\text{Sn}_2@\text{SnO}_2$ -6h and $\text{Co}_3\text{Sn}_2@\text{SnO}_2$ -12h CSHs.

Sample	R_e (Ω)	R_s (Ω)	R_{ct} (Ω)
$\text{Co}_3\text{Sn}_2@\text{SnO}_2$-6h CSHs -50	2.2	6.1	47.1
$\text{Co}_3\text{Sn}_2@\text{SnO}_2$-6 h CSHs- 500	2.9	18.7	23.5
$\text{Co}_3\text{Sn}_2@\text{SnO}_2$-12 h CSHs-50	3.9	8.5	31.7
$\text{Co}_3\text{Sn}_2@\text{SnO}_2$-12 h CSHs- 500	8.9	9.5	17.5

Table S3. The intensity ratio of the ex-situ XRD results at different charge/discharge states.

Ex-situ XRD state	New peak positions	Intensity of new peak	Intensity of peak at (002)	$I_{\text{new}}/I_{(002)}$
Pristine	26.5	26899.74	122097.73	0.22
Charged to 2.2 V	25.8	54977.53	324677.06	0.17
Charged to 3.0 V	25.8	60411.4	280574.28	0.22
Charged to 3.56 V	25.6	46141.53	114549.28	0.40
Charged to 4.5 V	25.6	57313.96	43298.23	1.32
Charged to 5.0 V	25.6	28873.21	15211.317	1.90
Discharged to 4.45 V	25.6	49069.08	27181.97	1.81
Discharged to 4.05 V	25.7	25671.86	14425.0211	1.78
Discharged to 2.57 V	25.83	46062.9	114392.025	0.40
Discharged to 2.0 V	25.83	50067.39	127068.239	0.39

Table S4. The intensity ratio (I_G/I_{G2}) of the ex-situ Raman results at different charge/discharge states.

Ex-situ Raman states	Intensity of peak at (1605 cm⁻¹) (I_G)	Intensity of peak at (1633 cm⁻¹) (I_{G2})	I_{G2}/I_G
Pristine	34806.79	20469.81	0.59
Charged to 2.2 V	41748.10	32051.39	0.77
Charged to 3.0 V	44634.23	37999.16	0.85
Charged to 3.56 V	41562.76	38580.46	0.93
Charged to 4.5 V	49601.94	46928.53	0.95
Charged to 5.0 V	51121.17	51049.57	1.0
Discharged to 4.45 V	31706.26	31052.23	0.99
Discharged to 4.05 V	46530.47	40577.28	0.87
Discharged to 2.57 V	49534.54	36827.44	0.74
Discharged to 2.0 V	42822.80	30208.09	0.71

Table S5. Performance comparison of this work and reported works for DIBs.

DIB Structure	Reversible capacity (mAh g ⁻¹)	Current density (mA g ⁻¹)	Cycle number	Estimated energy density (Wh kg ⁻¹)	Ref.
Graphite LiPF ₆ FEC-EMC Graphite	60	50	50	108	6
Li LiFTFSIPyr ₁₄ FTFSI Graphite	92	50	500	220	7
Si-compound 1M LiBF ₄ -PC Graphite	80	100	100	52	8
TiO ₂ 1M, LiPF ₆ - EC-DMC Graphite (1.5-3.7 V)	44	100	50	36	1
MoO ₃ 1M, LiPF ₆ - EC-DMC Graphite (1.5 3.5 V)	81	100	200	77	2
Al 4M, LiPF ₆ - EMC (2% VC) Graphite (3-5 V)	100	200	200	220	9
WS ₂ 1M, LiPF ₆ EC:EMC Graphite (0-4 V)	47	100	30	108	10
MnO 4M, LiPF ₆ EMC:VC Graphite (1.5-5 V)	95	186	300	326	11
Li 4M, LiPF ₆ - EMC:VC (LiNO ₃) Graphite (3.4-5 V)	69	400	1000	243	12
Co₃Sn₂@SnO₂ 1M LiPF₆- EC: DEC EG	90.0	300	200	334.5	This work

Table S6. The rate capability results of the DIBs.

Cycle	Current density (A g⁻¹)	Working voltage (V)	Charge capacity (mAh g⁻¹)	Discharge capacity (mAh g⁻¹)	CE (%)
1 st	0.1	3.71	645.0	185.0	28.91
7 th	0.1	3.66	244.3	140.9	61.59
8 th	0.2	3.65	174.6	112.8	83.91
13 th	0.3	3.66	106.9	91.8	91.06
18 th	0.5	3.68	81.0	71.3	95.64
23 th	0.7	3.70	66.3	60.5	97.12
28 th	1	3.67	54.6	49.5	98.00
33 th	2	3.65	50.3	49.5	99.81
38 th	3	3.60	30.2	30.0	99.33
43 th	0.1	-	138.3	107.6	77.8

References

1. A. K. Thapa, G. Park, H. Nakamura, T. Ishihara, N. Moriyama, T. Kawamura, H. Wang and M. Yoshio, *Electrochimica acta*, 2010, **55**, 7305-7309.
2. N. Gunawardhana, G.-J. Park, N. Dimov, A. K. Thapa, H. Nakamura, H. Wang, T. Ishihara and M. Yoshio, *Journal of Power Sources*, 2011, **196**, 7886-7890.
3. S. Bellani, F. Wang, G. Longoni, L. Najafi, R. Oropesa-Nunez, A. E. Del Rio Castillo, M. Prato, X. Zhuang, V. Pellegrini and X. Feng, *Nano letters*, 2018, **18**, 7155-7164.
4. J. H. Kim, N. P. Pieczonka and L. Yang, *ChemPhysChem*, 2014, **15**, 1940-1954.
5. X. Hu, G. Wang, B. Wang, X. Liu and H. Wang, *Chemical Engineering Journal*, 2019, **355**, 986-998.
6. J. A. Read, A. V. Cresce, M. H. Ervin and K. Xu, *Energy & Environmental Science*, 2014, **7**, 617-620.
7. P. Meister, V. Siozios, J. Reiter, S. Klamor, S. Rothermel, O. Fromm, H.-W. Meyer, M. Winter and T. Placke, *Electrochimica Acta*, 2014, **130**, 625-633.
8. H. Nakano, Y. Sugiyama, T. Morishita, M. J. S. Spencer, I. K. Snook, Y. Kumai and H. Okamoto, *Journal of Materials Chemistry A*, 2014, **2**, 7588-7592.
9. X. Zhang, Y. Tang, F. Zhang and C.-S. Lee, 2016, **6**, 1502588.
10. S. Bellani, F. Wang, G. Longoni, L. Najafi, R. Oropesa-Nuñez, A. E. Del Rio Castillo, M. Prato, X. Zhuang, V. Pellegrini, X. Feng and F. Bonaccorso, *Nano Letters*, 2018, **18**, 7155-7164.
11. L.-N. Wu, S.-Y. Shen, Y. Hong, C.-H. Shen, F.-M. Han, F. Fu, X. Zhou, L. Huang and S.-G. Sun, *ACS Applied Materials & Interfaces*, 2019, **11**.
12. L. N. Wu, J. Peng, Y. K. Sun, F. M. Han, Y. F. Wen, C. G. Shi, J. J. Fan, L. Huang, J. T. Li and S. G. Sun, *ACS Appl Mater Interfaces*, 2019, **11**, 18504-18510.